Supporting Information: A GaAs quantum dot in a parabolic microcavity tuned to ^{87}Rb D$_1$

Thomas Lettner,[*,†] Katharina D. Zeuner,[†] Eva Schöll,[†] Huiying Huang,[‡]

Selim Scharmer,[†] Saimon Filipe Covre da Silva,[‡] Samuel Gyger,[†]

Lucas Schweickert,[†] Armando Rastelli,[‡] Klaus D. Jöns,[*,†] and Val Zwiller[†]

†*Department of Applied Physics, Royal Institute of Technology, Albanova University Centre, Roslagstullsbacken 21, 106 91 Stockholm, Sweden*

‡*Institute of Semiconductor and Solid State Physics, Johannes Kepler University Linz, 4040, Austria*

E-mail: lettner@kth.se; klausj@kth.se

Contents

List of Figures

1 Statistical evaluation and collection efficiency enhancement

To statistically estimate the collection efficiency enhancement we record micro-photoluminescence spectra and integrate the intensities of all peaks originating from a single quantum dot. We perform this integration for 36 quantum dots in parabolic microcavities, 27 quantum dots from reference quantum dots in planar structures and 12 as-grown quantum dots to obtain 3 sets of data. We then determine the average integrated intensity and corresponding error for each data set and also the maximum data point (see Figure S1(a)). The parabolic microcavity achieves up to 7789.7 kcnts/s on the CCD, which is 21.6 times more than the average as-grown quantum dot (360 ± 64) kcnts/s and still 8.5 times brighter than the brightest as-grown quantum dot with 910.7 kcnts/s. The average parabolic microcavity quantum dot with (2189 ± 289) kcnts/s achieves an enhancement of 6.2 compared to the average as-grown quantum dot. In comparison, the reference dots, with on average (577 ± 74) kcnts/s, show only a factor 1.6 enhancement.

For the estimation of the collection efficiency we excite a bright parabolic microcavity quantum dot with a red laser diode with 80 MHz repetition rate and record the micro-photoluminescence spectrum. We identify the neutral exciton emission and integrate the emission with a 83 pm window (see Figure S1(b)), resulting in 105.672 kcnts/s. We characterize our setup with a tunable laser set to the emission wavelength of our quantum dot and use a pulse slicer to obtain a similar linewidth (inset in Figure S1(b)). We attenuate the laser in front of the spectrometer slit by 68.71 dB and obtain 75.988 kcnts/s integrated counts on the spectrometer for a measured power of 2.08 µW before the attenuation. From this, we derive a combined efficiency of spectrometer and CCD of $\eta_{Spec} = 6.8\%$. In the remaining detection path we measure the transmission of each optical component and then derive the efficiency to be $\eta_{Det} = 15.8\%$. The total setup efficiency is then the product $\eta_{Setup} = \eta_{Spec} * \eta_{Det} = 1.1\%$. By correcting the integrated exciton counts for the setup we

obtain 9606 kcnts/s into the first lens, which corresponds to a collection efficiency of 12 % from the exciton emission.

This collection efficiency gives a lower bound as we excited the quantum dot above-band, which causes the population of several states and not only the neutral exciton state used for this estimation. For example neutral and charged exciton states can not exist simultaneously, which in turn means, that the states are not excited by every excitation pulse (see Versteegh et al., Nat. Commun. 2014).
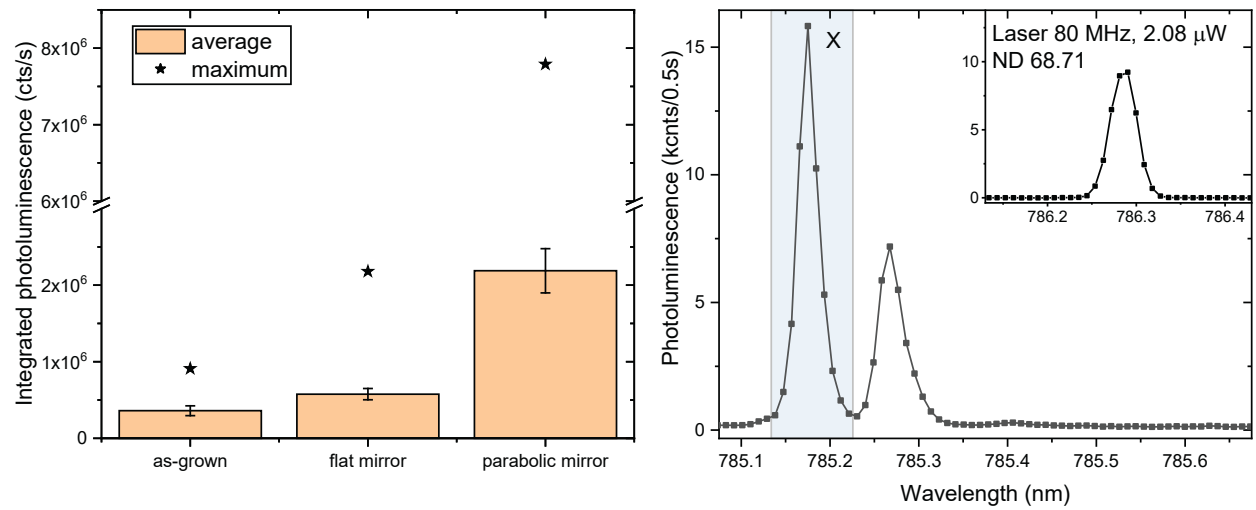

Figure S1: (a) Statistical evaluation: Bar plot of the integrated intensities of micro-photoluminescence spectra from parabolic microcavites, planar mirror reference and as-grown quantum dots. The bars represent the average value and error and the stars the maximum value in the data set. (b) Collection efficiency measurement: Micro-photoluminescence spectrum of the exciton emission of the bright parabolic microcavity quantum dot with integration window marked in blue. Inset: Spectrum of the 80 MHz repetion rate attenuated laser (2.08 µW, ND 68.71) for setup calibration.

2   Simulation of a laterally displaced dipole

The finite element method simulation allows us further to simulate an emitter that is not laterally in the center of the paraboloid. We select the paraboloid diameter d=1.45 μm, height h=500 nm and the dipole vertical position to match the focal length f=265 nm. Then we sweep the lateral position of the dipole towards the edge in 40 nm steps and record the collection efficiency, Purcell factor and far field emission pattern, for a dipole emission wavelength of λ=795 nm.

Figure S2(a) shows the collection efficiency for numerical apertures (NA) of 1.0, 0.8 and 0.4, and the Purcell factor as a function of the dipole displacement Δ from the center. Overall, the collection efficiency gradually drops until it falls below 0.2 for a displacement of up to 400 nm. The decrease occurs more rapidly for NA=0.8 and NA=0.4, where the value of 0.2 is already reached for a displacement of 120 nm and 80 nm, respectively. The Purcell factor on the contrary oscillates between 0.5 and 1.3 for λ=795 nm, where the maximum is reached for 240 nm.

Figure S2(b) visualizes the far field emission in a color-coded polar plot. The color scale is chosen in accordance with the far field emission for the centered emitter. The overall intensity is reduced by around 10 % and the maximum emission intensity is displaced from the center. In addition, the intensity profile is not gaussian anymore.

For our probabilistic approach of positioning the quantum dots we can now estimate the probability that we achieve a collection efficiency of more than 20 % into a lens with NA=0.8. The quantum dot has to lie within a radius of 120 nm corresponding to an area of $0.045\,\mu m^2$. The paraboloid radius and area are 530 nm and $0.88\,\mu m^2$, respectively, at the height of the quantum dot 265 nm above the apex. Therefore, the probability for a quantum dot to lie within 120 nm in the center is approximately 5 %.
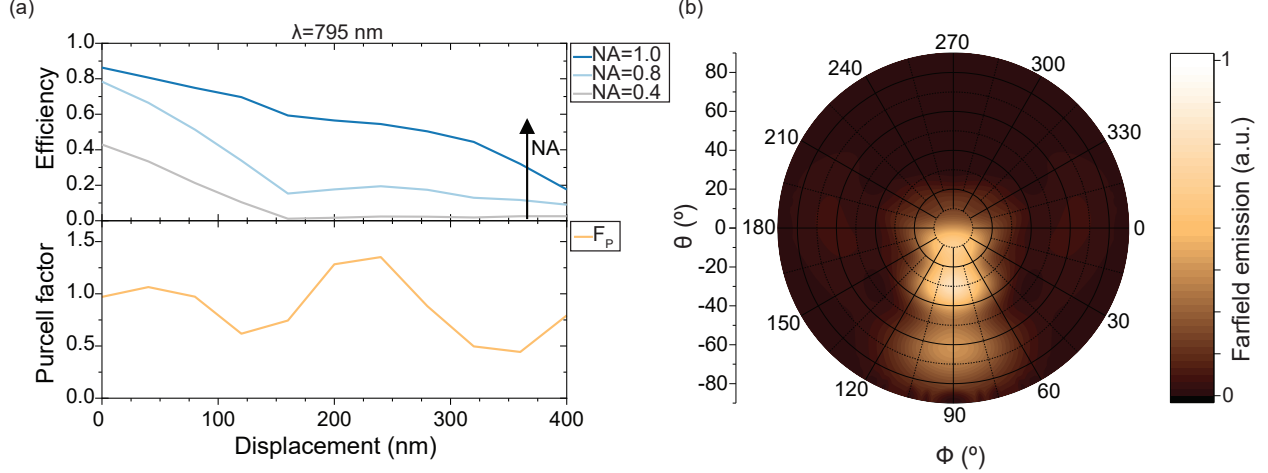
Figure S2: Simulation results for off-centered emitter, with (a) collection efficiency (top) for various numerical apertures (NAs) and Purcell factor (bottom) as a function of lateral dipole displacement Δ and (b) far field emission profile for the top hemisphere for $\Delta=80\,\mathrm{nm}$.

3 Atomic force microscopy characterization of reflown photoresist and etched paraboloid

We employ atomic force microscope measurements (see Fig. S3) to characterize the height profile and roughness of the photoresist (Fig. S3(a-c)) and the etched structure (Fig. S3(d-f)). In Fig. S3(a,d) we show the height data with lighting from the sides. The etched parabola features a flat $0.5\,\mu\mathrm{m}$ wide apex which we attribute to incomplete removal of the photoresist during the dry etching and subsequent cleaning. In Fig. S3(b,e) we show the color-coded height data and a fit (dashed lines) to a paraboloid. In case of the etched paraboloid we consider for the fit only the top $0.5\,\mu\mathrm{m}$ of the paraboloid by clipping the rest, because everything below is beyond the sacrificial layer and not part of the final device. We observe that our paraboloids appear to be not fully round at the base, therefore, our fit model allows for two in-plane diameters (major- and minor axis of an ellipse). The resulting diameters for the fit of the etched paraboloid are $1.611\,\mu\mathrm{m}$ and $1.386\,\mu\mathrm{m}$, which corresponds to a roundness of $(84\pm0.5)\%$ as calculated from the ratio of the two diameters. In comparison, the roundness of the photoresist is $(95\pm0.5)\%$. To quantify the agreement of our model with the measured atomic force microscope data, we subtract the data from the fit and obtain a

height difference map (see Fig. S3(c,f)). We find that the deviations are at most 28 nm from the perfect shape for the etched paraboloids.

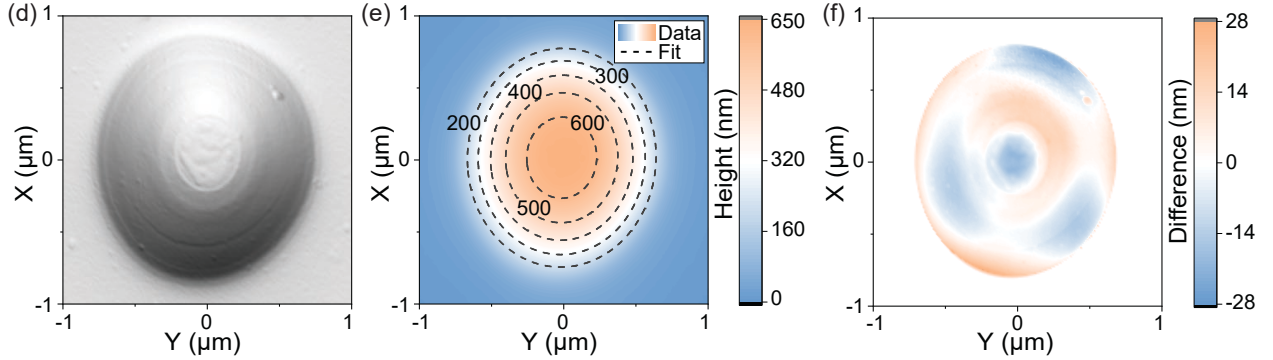Reflown photoresist:
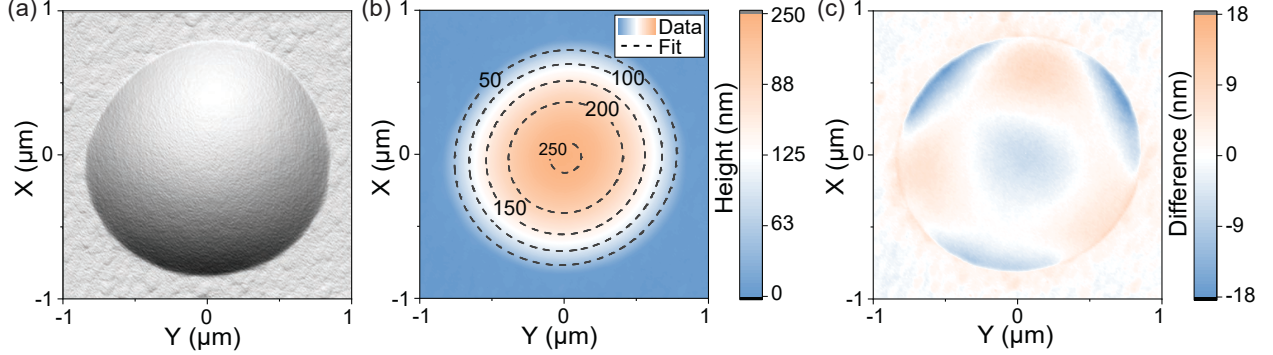
Etched paraboloid:

Figure S3: Atomic force microscopy measurement results for photoresist reflow (a-c) and etched paraboloid (d-f). (a,d) Height data visualization with lighting from the side. (b,e) Color-coded height data and fit (dashed) to a model paraboloid. (c,f) Color-coded difference map obtained from subtraction of data and fit.

4   Simulation with atomic force microscopy data

To estimate how well a real life device could perform at best with our current fabrication precision, we import the atomic force microscopy height profile shown in Fig. S3 (d) and replace the previously used perfect parabola, while keeping the emitter centered. The results are shown in Fig. S4(a) where we plot the far field emission profile in the same range as in the main text. Compared to the perfect structure, the main intensity of the far field is now slightly off-centered which we attribute to the slight asymmetry of the real structure.

Nevertheless, the collection efficiency plotted in Fig. S4(b) reaches up to 65 % for an NA of 0.8 and 63.5 % for 795 nm. We also notice that the overall shape of the curve appears more smooth and flat, which we attribute to the surface roughness smearing out the cavity effects.
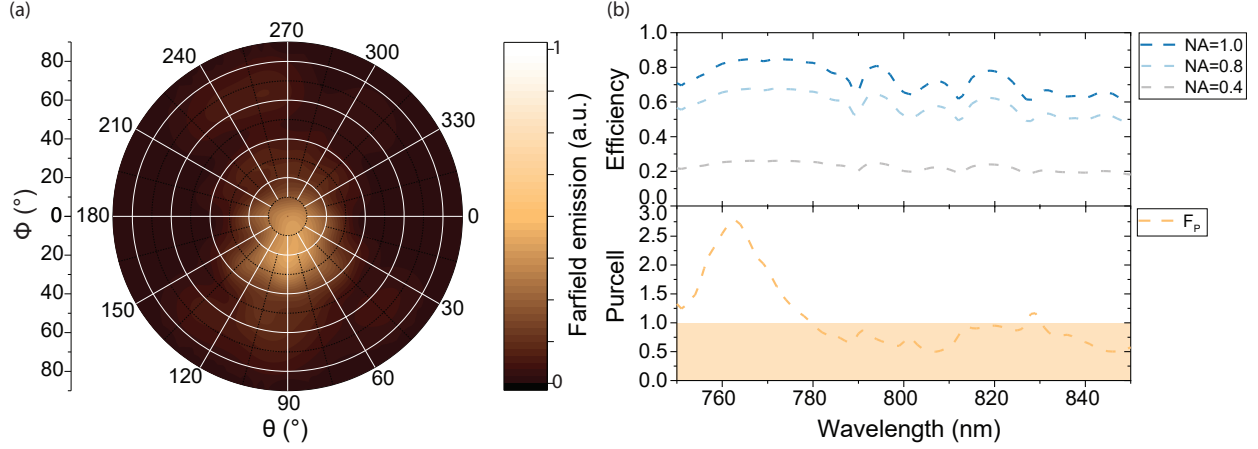

Figure S4: Simulation for imported atomic force microscopy data from S3. (a) Far field for simulation with imported atomic force microscopy data with centered emitter. (b) Collection efficiencies (top) for various numerical apertures (NAs) and Purcell factor (bottom) as a function of wavelength.